Computing Geodesic Paths Encoding a Curvature Prior for Curvilinear Structure Tracking

Da Chen · Jean-Marie Mirebeau · Minglei Shu · Laurent D. Cohen

Abstract In this paper, we introduce an efficient method for computing curves minimizing a variant of the Euler-Mumford elastica energy, with fixed endpoints and tangents at these endpoints, where the bending energy is enhanced with a user defined and data-driven scalar-valued term referred to as the curvature prior. In order to guarantee that the globally optimal curve is extracted, the proposed method involves the numerical computation of the viscosity solution to a specific static Hamilton-Jacobi-Bellman (HJB) partial differential equation (PDE). For that purpose, we derive the explicit Hamiltonian associated to this variant model equipped with a curvature prior, discretize the resulting HJB PDE using an adaptive finite difference scheme, and solve it in a single pass using a generalized Fast-Marching method. In addition, we also present a practical method for estimating the curvature prior values from image data, designed for the task of accurately tracking curvilinear structure centerlines. Numerical experiments on synthetic and real image data illustrate the advantages of the considered variant of the elastica model with a prior curvature enhancement in complex scenarios where challenging geometric structures appear.

Da Chen
Shandong Artificial Intelligence Institute, Qilu University of Technology (Shandong Academy of Sciences), 250014 Jinan, China.
E-mail: dachen.cn@hotmail.com

Jean-Marie Mirebeau
Department of Mathematics, Centre Borelli, ENS Paris-Saclay, CNRS, University Paris-Saclay, 91190, Gif-sur-Yvette, France.
E-mail: jean-marie.mirebeau@math.u-psud.fr

Minglei Shu
Shandong Artificial Intelligence Institute, Qilu University of Technology (Shandong Academy of Sciences), 250014 Jinan, China.
E-mail: shuml@sdas.org

Laurent D. Cohen
University Paris Dauphine, PSL Research University, CNRS, UMR 7534, CEREMADE, 75016 Paris, France
E-mail: cohen@ceremade.dauphine.fr

1 Introduction

Computing globally optimal geodesic curves, in domains equipped with complex metric cost functions, is a task efficiently achieved by solving the so-called eikonal equation, which is at the foundation of a line of works in the modeling of curvilinear shapes (Sethian, 1999; Peyré et al, 2010). Second-order geodesic models featuring curvature regularization allow imposing particular geometric priors (e.g. rigidity and smoothness) to the minimal geodesic paths, whose computation hence has become a core step to numerous practical applications. Typical examples include image analysis (Chen et al, 2017; Bekkers et al, 2015a), computer vision problems involving visual curve completion (Ben-Shahar and Ben-Yosef, 2014; Parent and Zucker, 1989) and perceptual grouping (Bekkers et al, 2018; Wertheimer, 1938), the study of optical illusions (Franceschiello et al, 2019), and robot motion planing (Mirebeau and Portegies, 2019; Kimmel and Sethian, 2001). This work is motivated by the fact that curvilinear structures exhibit significant geometric features such as orientation and curvature, which can be leveraged as crucial cues for computing geodesic paths to efficiently delineate these elongated shapes.

Approaches to computing globally optimal paths connecting two disjoint sets can be backtracked to Dijkstra's shortest path algorithm (Dijkstra, 1959) in a finite graph. However, such a discrete setting may lead to metrication errors, especially for applications in image analysis. In order to address this issue, Cohen and Kimmel introduced a minimal geodesic model (Cohen and Kimmel, 1997) founded in a continuous PDE domain, and established the connection between the minimization of an energy defined as a weighted curve length (Caselles et al, 1997) and the viscosity solution to a static first-order HJB PDE. As a consequence, the computation of minimal geodesic paths is transferred to numerically solving the HJB PDE, which is efficiently addressed via Sethian's pioneering work (Sethian, 1996, 1999) the Fast-Marching method.

The original geodesic model (Cohen and Kimmel, 1997) measures the length of regular curves in an isotropic manner, using weights depending on the local curve position but not on its orientation, which limits its practical applications. The introduction of anisotropic geometric models, and measures

of path length depending on the orientation in a user-defined manner, is an important extension to the original geodesic model, which has deeply extended its applicable scope, leading to successful applications in image analysis and computer vision (Melonakos et al, 2008). For instance, curvilinear structure tracking can take advantage of anisotropic Riemannian models, by enhancing the geodesic metric with anisotropy features extracted from the elongated structures present in the processed image (Parker et al, 2002; Benmansour and Cohen, 2011; Jbabdi et al, 2008). Chen et al (2016) proposed to address the region-based active contour problem (Mumford and Shah, 1989) by computing the minimal geodesic path associated to a Randers metric (Randers, 1941) featuring a data-driven drift term. For geodesic models involving anisotropic metrics, the classical Fast-Marching method (Sethian, 1996) is no longer suitable for estimating the solutions to the respective HJB PDEs (Sethian and Vladimirsky, 2001, 2003). In order to bridge this gap, Mirebeau introduced variants of the Fast-Marching method which rely on adaptive stencil systems depending on the associated metrics, based on either the geometric tool of Lattice basis reduction (Mirebeau, 2014b,a) or the Voronoi's first reduction technique (Mirebeau, 2019, 2018). In practice, those state-of-the-art generalized anisotropic Fast-Marching methods can address various anisotropic geodesic models, while achieving sufficient accuracy and requiring a low computational cost.

Second-order geodesic models, which use the path curvature as a regularizer of the weighted curve length, can be regarded as limit cases of anisotropic models defined over the configuration space of positions and orientations, see (Chen et al, 2017; Duits et al, 2018; Bekkers et al, 2015a; Mirebeau, 2018) for significant examples. Following the optimal control framework, the Euler-Mumford elastica, Reeds–Shepp car and Dubins car problems are respectively connected to the associated HJB PDEs, yielding efficient Fast-Marching schemes for finding curvature-penalized optimal curves (Mirebeau, 2018). An extension of these models allows computing curves which are boundaries of convex shapes, by controlling the sign of the curvature and the winding number of the path (Chen et al, 2021). In these works, the curvature penalization is regarded as a regularization term, whose importance is delicately balanced with an image data term, following the general principles of data fitting.

In practice, unfortunately, striking a good balance between the curvature regularization and the image data terms remains a challenging problem for these second-order geodesic models (Chen et al, 2017; Duits et al, 2018; Mirebeau, 2018), particularly in the presence of crossing structures, strongly bent segments, and complex image background content. In general, assigning high importance weights to curvature regularization usually corresponds to optimal paths favoring low curvature. On the other hand, such a setting may in turn introduce a bias to the underlying strongly curved segments, thus giving rise to unexpected results. Fig. 1 illustrates an example in an aerial image, where the goal is to extract a road joining two given points (red and blue dots), see Fig. 1a. In Fig. 1b, one can see that the geodesic path derived from the classical Euler-Mumford elastica model (Chen et al, 2017; Mirebeau, 2018) suffers from a shortcut problem, due to the unbalanced importance of the weights associated to the curva-

ture regularization and to the image data. This shortcoming of the classical elastica model prevents its practical applications in complex scenarios. An alternative approach, explored in this paper and motivated by the drawback as mentioned above, is to compute geodesic paths whose curvature approximates some data-driven prior reference values and more generally to introduce data information in the new curvature term. An additional contribution is a collection of techniques to estimate these prior curvature values from the image data, and to extend and preprocess them for their use as an enhancement to the geodesic model. Fig. 1c illustrates an optimal path from the variant of the elastica model, equipped with a suitable curvature prior which enables the accurate extraction of the target road.

In (Mirebeau and Portegies, 2019), the authors illustrated how geodesic paths with a type of curvature prior could be computed using a modification of the Hamiltonian Fast-Marching (HFM) method (Mirebeau, 2018, 2019). However, the mathematical PDE framework, the construction of the numerical scheme, and the application scope of the geodesic models with embedded curvature prior were not investigated. In this paper, we describe the Hamiltonian of a variant of the Euler-Mumford elastica model featuring a curvature prior enhancement, and we illustrate related objects known as control sets. The Hamiltonian of this variant of the classical elastica model, referred to as the *curvature prior elastica model*, is then discretized, leading to a numerical method for solving the corresponding static first-order HJB PDE, and thus computing the globally optimal geodesic paths. Finally, we introduce a practical method for estimating the curvature prior values, designed to improve the performance of tracking curvilinear structures from challenging image data.

The remainder of this manuscript is organized as follows. We first review the classical Euler-Mumford elastica model, including the expression of the associated HJB PDE which is posed over the configuration space of positions and orientations, and the computation of the relevant minimal geodesic paths. Then we present the core of this work: the derivation of the Hamiltonian of a variant of the elastica model equipped with a curvature prior, the relevant static HJB PDE, and its implementation in the application of curvilinear structure tracking. Eventually, we present experimental results conducted on both synthetic and real images.

2 The Euler-Mumford Elastica Model

2.1 Background

The celebrated Euler-Mumford elastica model (Mumford, 1994; Nitzberg, 1990) characterizes smooth curves which minimize a functional featuring a length term and a bending energy term, in other words a curvature penalization. Let $\kappa : [0,1] \to \mathbb{R}$ be the curvature of a smooth curve $\gamma : [0,1] \to \Omega$ with non-vanishing velocity, where $\Omega \subset \mathbb{R}^2$ is a bounded domain. Given a data-driven cost function $\tilde{\psi} : \Omega \times \mathbb{R}^2 \to]0, \infty[$, the energy functional considered in the classical Euler-Mumford elastica model reads

$$\int_0^1 \tilde{\psi}\left(\gamma(u), \gamma'(u)/\|\gamma'(u)\|\right)(1 + \beta^2 \kappa(u)^2)\|\gamma'(u)\|du, \quad (1)$$
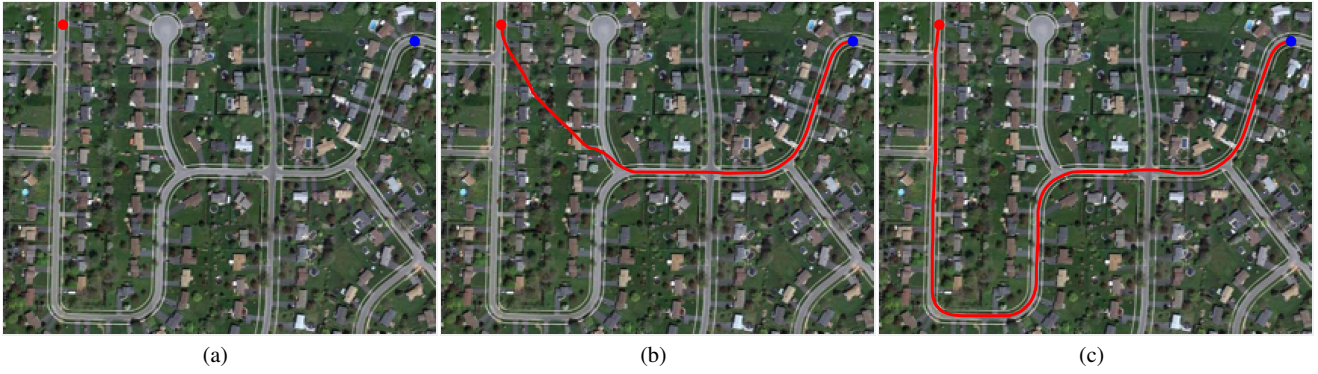
Fig. 1 Illustration of the extraction of geodesic paths from an aerial image. **a** The original image, where the red and blue dots represent the two endpoints of the target structure. **b** and **c** Physical projections of the minimal geodesic paths for the Euler-Mumford elastica model and the variant of the elastica model with a curvature prior enhancement respectively.

where γ' is the first-order derivative of the curve γ, and $\|\cdot\|$ denotes the standard Euclidean norm over the space $\mathbb{R}^2$. The constant parameter $\beta > 0$ controls the relative importance of the bending energy term $\kappa(u)^2$, which penalizes curvature, w.r.t. the penalization of path length. By construction, Eq. (1) is invariant under smooth increasing re-parametrizations of the curve γ, and the second argument of $\tilde{\psi}$ is the unit tangent vector to the path. In the special case where $\tilde{\psi}$ is constant, the curves γ for which Eq. (1) is extremal correspond to the rest positions of elastic rods of suitable length (with their endpoints clamped), however this physical interpretation is lost for non-constant $\tilde{\psi}$.

2.2 Reformulation via Orientation Lifting

A widely used strategy for addressing the classical Euler-Mumford elastica optimal curve problem is to lift a planar smooth curve γ into the higher dimensional configuration space $\mathbb{M} := \Omega \times \mathbb{S}^1$ of positions and orientations, see (Chen et al, 2017; Duits et al, 2018; Chambolle and Pock, 2019), where $\mathbb{S}^1 := \mathbb{R}/2\pi\mathbb{Z}$ denotes the angular domain. In other words $\mathbb{S}^1 = [0, 2\pi[$ with periodic boundary conditions, and we can parametrize the unit circle via the unit vector $\dot{n}(\theta) := (\cos\theta, \sin\theta)$ for any angle $\theta \in \mathbb{S}^1$. Furthermore, we denote by $\mathbb{E} := \mathbb{R}^2 \times \mathbb{R}$ the tangent vector space to $\mathbb{M}$, and by $\mathbb{E}^*$ the dual vector space of $\mathbb{E}$. Recall that $\gamma : [0, 1] \to \Omega$ is a smooth curve with non-vanishing velocity. Following the literature (Chen et al, 2017; Mirebeau, 2018; Duits et al, 2018), an orientation-lifted curve $\boldsymbol{\rho} = (\gamma, \eta) : [0, 1] \to \mathbb{M}$, whose *physical projection* is the given planar curve γ, can be constructed by introducing an *angular function* $\eta : [0, 1] \to \mathbb{S}^1$ such that

$$\gamma'(u) = \dot{n}(\eta(u))\|\gamma'(u)\|, \quad \forall u \in [0, 1]. \quad (2)$$

This leads to an alternative representation of the curvature

$$\kappa(u) = \frac{\eta'(u)}{\|\gamma'(u)\|}. \quad (3)$$

Inserting this expression of the curvature κ into the energy defined in Eq. (1) yields an equivalent formula, measured along an orientation-lifted curve $\boldsymbol{\rho} = (\gamma, \eta)$ whose components γ and η obey Eq. (2):

$$\mathcal{L}(\boldsymbol{\rho}) := \int_0^1 \psi(\gamma(u), \eta(u)) \left(\|\gamma'(u)\| + \frac{\beta^2 \eta'(u)^2}{\|\gamma'(u)\|} \right) du, \quad (4)$$

where $\psi : \mathbb{M} \to]0, \infty[$ is a positive cost function defined by

$$\psi(x, \theta) := \tilde{\psi}(x, \dot{n}(\theta)).$$

For the task of curvilinear structure tracking, as considered in this work, the value of $\psi(x, \theta)$ should be relatively low in case the physical position x is inside a curvilinear structure and the direction $\dot{n}(\theta)$ matches its local geometry at the position x, i.e. $\dot{n}(\theta)$ is approximately tangent to its centerline at x. Fig. 2 shows an example for the cost function ψ derived from an image that consists of curvilinear structures. The construction and the numerical computation of ψ is presented in Eq. (25) below, and relies on a tool known as the orientation score.

2.3 Elastica Metric and Control Sets

The energy $\mathcal{L}(\boldsymbol{\rho})$ formulated in Eq. (4) can be expressed in terms of a degenerate geodesic metric (Chen et al, 2017; Mirebeau, 2018), denoted by $\mathcal{F} : \mathbb{M} \times \mathbb{E} \to [0, +\infty]$ and referred to as the *elastica metric*. For any point $\mathbf{x} = (x, \theta)$ and any non-zero vector $\dot{\mathbf{x}} = (\dot{x}, \dot{\theta})$ this elastica metric is defined as

$$\mathcal{F}(\mathbf{x}, \dot{\mathbf{x}}) := \begin{cases} \|\dot{x}\| + \dfrac{(\beta\dot{\theta})^2}{\|\dot{x}\|}, & \text{if } \dot{x} = \dot{n}(\theta)\|\dot{x}\|, \\ +\infty, & \text{otherwise.} \end{cases} \quad (5)$$

Note that this metric is not symmetric, since $\mathcal{F}(\mathbf{x}, \dot{\mathbf{x}}) \neq \mathcal{F}(\mathbf{x}, -\dot{\mathbf{x}})$ in general in view of the non-linear constraint $\dot{x} = \dot{n}(\theta)\|\dot{x}\|$, and thus the corresponding distance defined below (see Eq. (11)) is likewise non-symmetric. Such asymmetric objects are often referred to as quasi-metrics and quasi-distances, but the prefix "quasi-" is dropped in this paper for the sake of readability.

Several mathematical objects can be attached to such a metric. The *control sets* $\mathcal{B}(\mathbf{x}) \subset \mathbb{E}$, for all points $\mathbf{x} \in \mathbb{M}$, allow visualizing the geometry, see Fig. 3, and are defined as

$$\mathcal{B}(\mathbf{x}) := \{\dot{\mathbf{x}} \in \mathbb{E} \mid \mathcal{F}(\mathbf{x}, \dot{\mathbf{x}}) \leq 1\}. \quad (6)$$

The *Hamiltonian* $\mathcal{H} : \mathbb{M} \times \mathbb{E}^* \to [0, \infty[$ is involved in the numerical computation of optimal geodesic paths through the HJB PDE, as formulated in next subsection, and is defined for any co-vector $\hat{\mathbf{x}} \in \mathbb{E}^*$ as

$$\mathcal{H}(\mathbf{x}, \hat{\mathbf{x}}) := \frac{1}{2} \left(\max_{\dot{\mathbf{x}} \in \mathcal{B}(\mathbf{x})} \langle \hat{\mathbf{x}}, \dot{\mathbf{x}} \rangle \right)^2. \quad (7)$$
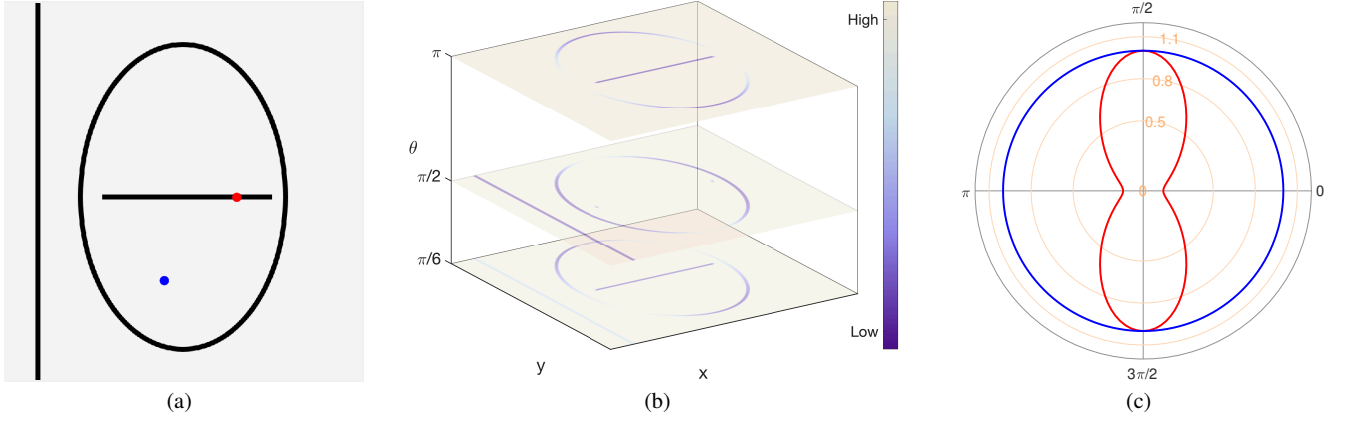
Fig. 2 Visualizing the cost function ψ in a synthetic example. **a** The original image consisting of curvilinear structures, where the red and blue dots indicate two sampled points. **b** Visualizing the cost function $\psi(\cdot, \theta)$ at three slices corresponding to the angles $\theta = \pi/6$, $\pi/2$ and π. **c** Visualizing the cost function $\psi(x, \cdot)$ at two sampled points in polar coordinates, where the red and blue lines correspond to plots of the values at the red and blue dots, respectively.

In the special case of the elastica metric, one can use Eq. (5) to obtain the explicit expressions of the control sets and Hamiltonian, see (Mirebeau, 2018) for the details of this computation. Specifically, for any point $\mathbf{x} = (x, \theta) \in \mathbb{M}$ one has

$$\mathcal{B}(\mathbf{x}) = \left\{ (\dot{x}, \dot{\theta}) \in \mathbb{E} \mid \dot{x} = \dot{\mathrm{n}}(\theta)\|\dot{x}\|, \left(\|\dot{x}\| - \frac{1}{2} \right)^2 + \beta^2 \dot{\theta}^2 \leq \frac{1}{4} \right\}. \tag{8}$$

For any co-vector $\hat{\mathbf{x}} = (\hat{x}, \hat{\theta}) \in \mathbb{E}^*$ one obtains

$$\mathcal{H}(\mathbf{x}, \hat{\mathbf{x}}) = \frac{1}{8} \left(\langle \hat{x}, \dot{\mathrm{n}}(\theta) \rangle + \sqrt{\langle \hat{x}, \dot{\mathrm{n}}(\theta) \rangle^2 + (\hat{\theta}/\beta)^2} \right)^2. \tag{9}$$

The following equivalent expression of the Hamiltonian, in integral form, is established in Mirebeau (2018)

$$\mathcal{H}(\mathbf{x}, \hat{\mathbf{x}}) = \frac{3}{8} \int_{-\pi/2}^{\pi/2} \langle \hat{\mathbf{x}}, (\dot{\mathrm{n}}(\theta) \cos \varphi, \beta^{-1} \sin \varphi) \rangle_+^2 \cos \varphi \, d\varphi, \tag{10}$$

where $\langle \cdot, \cdot \rangle_+ := \max\{0, \langle \cdot, \cdot \rangle\}$ is the positive part of the Euclidean scalar product $\langle \cdot, \cdot \rangle$. Here and below we denote the vector $\dot{\mathrm{n}}(\theta, a) := (\dot{\mathrm{n}}(\theta), a) \in \mathbb{E}$ for any angle $\theta \in \mathbb{S}^1$ and any scalar $a \in \mathbb{R}$, and observe that in particular $\langle \hat{x}, \dot{\mathrm{n}}(\theta) \rangle = \langle \hat{\mathbf{x}}, \dot{\mathrm{n}}(\theta, 0) \rangle$.

2.4 Computing Elastica Geodesic Paths

Consider a fixed source point $\mathbf{s} \in \mathbb{M}$ and an arbitrary target point $\mathbf{x} \in \mathbb{M}$, thus defining initial and final planar endpoints and tangent path directions. The classical Euler-Mumford elastica geodesic model (Chen et al, 2017; Mirebeau, 2018) aims to track a minimal geodesic path $\mathcal{G}_{\mathbf{s}, \mathbf{x}} : [0, 1] \to \mathbb{M}$ which links from the source point $\mathbf{s}$ to the target point $\mathbf{x}$ (i.e. $\mathcal{G}_{\mathbf{s}, \mathbf{x}}(0) = \mathbf{s}$, $\mathcal{G}_{\mathbf{s}, \mathbf{x}}(1) = \mathbf{x}$) and minimizes the energy $\mathcal{L}$ formulated in Eq. (4). For that purpose, we first consider the set $\mathrm{Lip}([0, 1], \mathbb{M})$ of all Lipschitz continuous curves $\boldsymbol{\rho} : [0, 1] \to \mathbb{M}$ as the search space of geodesic paths. The

minimization of the energy $\mathcal{L}$ yields a geodesic distance map $\mathcal{D}_{\mathbf{s}} : \mathbb{M} \to [0, \infty)$, defined as

$$\mathcal{D}_{\mathbf{s}}(\mathbf{x}) := \inf_{\boldsymbol{\rho} \in \mathrm{Lip}([0,1], \mathbb{M})} \mathcal{L}(\boldsymbol{\rho}), \quad s.t. \begin{cases} \boldsymbol{\rho}(0) = \mathbf{s}, \\ \boldsymbol{\rho}(1) = \mathbf{x}. \end{cases} \tag{11}$$

The geodesic distance map $\mathcal{D}_{\mathbf{s}}$ is a potentially discontinuous viscosity solution to the first-order static HJB PDE (Bardi and Capuzzo-Dolcetta, 2008)

$$\begin{cases} \mathcal{H}(\mathbf{x}, d\mathcal{D}_{\mathbf{s}}(\mathbf{x})) = \frac{1}{2} \psi(\mathbf{x})^2, \ \forall \mathbf{x} \in \mathbb{M} \backslash \{\mathbf{s}\}, \\ \mathcal{D}_{\mathbf{s}}(\mathbf{s}) = 0, \end{cases} \tag{12}$$

where $d\mathcal{D}_{\mathbf{s}}$ denotes the differential of the geodesic distance map $\mathcal{D}_{\mathbf{s}}$. Outflow boundary conditions are applied on $\partial \mathbb{M}$.

A *reversely parametrized* minimal geodesic path $\tilde{\mathcal{G}}$, starting from a given target point $\mathbf{x}$ and going back to the source point $\mathbf{s}$, can be obtained by solving the following gradient descent ordinary differential equation (ODE), known as the *geodesic backtracking* ODE

$$\tilde{\mathcal{G}}'(u) = -\partial_2 \mathcal{H}(\tilde{\mathcal{G}}(u), d\mathcal{D}_{\mathbf{s}}(\tilde{\mathcal{G}}(u))), \tag{13}$$

with initial condition $\tilde{\mathcal{G}}(0) = \mathbf{x}$, and where $\partial_2 \mathcal{H} := \partial \mathcal{H}(\mathbf{x}, \hat{\mathbf{x}})/\partial \hat{\mathbf{x}}$. By construction, this path is well-defined up to the minimal arrival time $T := \mathcal{D}_{\mathbf{s}}(\mathbf{x})$, and $\tilde{\mathcal{G}}(T) = \mathbf{s}$ is the source point. The reparametrization $\mathcal{G}_{\mathbf{s}, \mathbf{x}}(u) := \tilde{\mathcal{G}}(T(1 - u))$ yields a minimal geodesic path $\mathcal{G}_{\mathbf{s}, \mathbf{x}} : [0, 1] \to \mathbb{M}$ such that $\mathcal{G}_{\mathbf{s}, \mathbf{x}}(0) = \mathbf{s}$ and $\mathcal{G}_{\mathbf{s}, \mathbf{x}}(1) = \mathbf{x}$.

3 Curvature Prior Elastica Model: A Variant of the Classical Euler-Mumford Elastica Model

In this section, we present a variant of the Euler-Mumford elastica geodesic model, favoring minimal geodesic paths whose curvature remains close to a prior reference value, defined pointwise. For comparison, the classical Euler-Mumford elastica model (Chen et al, 2017), which favors geodesic paths of low curvature, corresponds to the special case where these prior values are defined as zero uniformly over the domain $\mathbb{M}$.

3.1 Formalism

We begin by formulating a new curvature penalization term, which involves a scalar-valued function $\omega : \mathbb{M} \to \mathbb{R}$. For a smooth curve γ with curvature κ, we consider

$$\tilde{\kappa}(u) = \kappa(u) - \omega\big(\gamma(u), \eta(u)\big), \qquad (14)$$

where the angle $\eta(u) \in \mathbb{S}^1$ reflects the tangent path direction for all $u \in [0, 1]$, see Eq. (2). In this model, the function ω is referred to as the curvature prior map. For the purposes of curvilinear structure tracking, as considered in this paper the value $\omega(x, \theta)$ may be defined as the curvature of a reference curve passing nearby the position x, with a tangent orientation close to θ, and obtained using an independent skeletonization procedure, see Eq. (24).

We consider the variant of the Euler-Mumford elastic energy involving the curvature prior map ω and defined as:

$$\int_0^1 \psi(\gamma(u), \eta(u)) \left(1 + (\beta\tilde{\kappa}(u))^2\right) \|\gamma'(u)\| du. \qquad (15)$$

For an orientation-lifted curve $\boldsymbol{\rho} = (\gamma, \eta)$ satisfying Eq. (2), the corresponding quantity is defined as

$$\mathfrak{L}(\boldsymbol{\rho}) := \int_0^1 \psi(\boldsymbol{\rho}) \left(1 + \beta^2 \left(\frac{\eta'}{\|\gamma'\|} - \omega(\boldsymbol{\rho})\right)^2\right) \|\gamma'\| du. \qquad (16)$$

The energy $\mathfrak{L}$ leads to a new metric $\mathfrak{F} : \mathbb{M} \times \mathbb{E} \to [0, \infty]$ (Mirebeau and Portegies, 2019)

$$\mathfrak{F}(\mathbf{x}, \dot{\mathbf{x}}) := \begin{cases} \|\dot{x}\| + \frac{\beta^2(\dot{\theta} - \omega(\mathbf{x})\|\dot{x}\|)^2}{\|\dot{x}\|}, & \text{if } \dot{x} = \dot{\mathrm{n}}(\theta)\|\dot{x}\|, \\ \infty, & \text{otherwise,} \end{cases} \qquad (17)$$

where $\mathbf{x} = (x, \theta) \in \mathbb{M}$, and where $\dot{\mathbf{x}} = (\dot{x}, \dot{\theta}) \in \mathbb{E}$, with the convention $\mathfrak{F}(\mathbf{x}, \mathbf{0}) = 0$. The energy $\mathfrak{L}(\boldsymbol{\rho})$ can therefore be reformulated as

$$\mathfrak{L}(\boldsymbol{\rho}) = \int_0^1 \psi(\boldsymbol{\rho}(u)) \mathfrak{F}(\boldsymbol{\rho}(u), \boldsymbol{\rho}'(u)) du.$$

Path globally minimizing this energy can be obtained, similarly to the classical case and following the general principles of optimal control, by applying the geodesic backtracking ODE to the viscosity solution of a HJB PDE, both involving a suitably modified Hamiltonian described in the next section.

3.2 Transformation of the Hamiltonian and Control Set

In order to describe our variant of the classical elastica model with curvature prior, we briefly adopt a more general point of view. A (sub-Finslerian) metric on the domain $\mathbb{M}$ is a mapping $\mathcal{F} : \mathbb{M} \times \mathbb{E} \to [0, \infty]$, obeying $\mathcal{F}(\mathbf{x}, \lambda\dot{\mathbf{x}}) = \lambda\mathcal{F}(\mathbf{x}, \dot{\mathbf{x}})$ for any $\mathbf{x} \in \mathbb{M}$, $\dot{\mathbf{x}} \in \mathbb{E}$, $\lambda > 0$, satisfying $\mathcal{F}(\mathbf{x}, \mathbf{0}) = 0$, and such that the control sets $\mathcal{B}(\mathbf{x})$ defined by Eq. (6) are non-empty, convex, compact, and depend continuously on the base point $\mathbf{x} \in \mathbb{M}$ w.r.t. the Hausdorff distance (Chen et al, 2017). Some control sets obeying these properties are illustrated in the right column of Fig. 3, where the corresponding *Hamiltonian* $\mathcal{H}$ is defined by Eq. (7).

Proposition 3.1 *Let $\mathcal{F}$ be a metric on the domain $\mathbb{M}$, let $\mathcal{L}_{\mathbf{x}} : \mathbb{E} \to \mathbb{E}$ be a linear invertible map depending continuously on the parameter $\mathbf{x} \in \mathbb{M}$, and let $\mathfrak{F}(\mathbf{x}, \dot{\mathbf{x}}) := \mathcal{F}(\mathbf{x}, \mathcal{L}_{\mathbf{x}}\dot{\mathbf{x}})$ for all $\dot{\mathbf{x}} \in \mathbb{E}$. Then $\mathfrak{F}$ is a metric on $\mathbb{M}$, and the corresponding control sets $\mathfrak{B}$ and Hamiltonian $\mathfrak{H}$ are obtained from those of the metric $\mathcal{F}$ denoted $\mathcal{B}$ and $\mathcal{H}$ as follows*

$$\mathfrak{B}(\mathbf{x}) = \mathcal{L}_{\mathbf{x}}^{-1}\mathcal{B}(\mathbf{x}), \qquad \mathfrak{H}(\mathbf{x}, \hat{\mathbf{x}}) = \mathcal{H}(\mathbf{x}, \mathcal{L}_{\mathbf{x}}^{-\top}\hat{\mathbf{x}}).$$

Proof The expression of the transformed control set $\mathfrak{B}(\mathbf{x}) \subset \mathbb{E}$ follows from the series of equivalences:

$$\dot{\mathbf{x}} \in \mathfrak{B}(\mathbf{x}) \Leftrightarrow \mathcal{F}(\mathbf{x}, \mathcal{L}_{\mathbf{x}}\dot{\mathbf{x}}) \leq 1 \Leftrightarrow \mathcal{L}_{\mathbf{x}}\dot{\mathbf{x}} \in \mathcal{B}(\mathbf{x}) \Leftrightarrow \dot{\mathbf{x}} \in \mathcal{L}_{\mathbf{x}}^{-1}\mathcal{B}(\mathbf{x}).$$

By linearity of $\mathcal{L}_{\mathbf{x}}^{-1}$, the set $\mathfrak{B}(\mathbf{x})$ is like $\mathcal{B}(\mathbf{x})$ non-empty, convex, and compact. In addition, the set $\mathfrak{B}(\mathbf{x})$ depends continuously on the point $\mathbf{x} \in \mathbb{M}$, by continuity of $\mathcal{B}(\mathbf{x})$ and $\mathcal{L}_{\mathbf{x}}^{-1}$. Noting that $\mathfrak{F}(\mathbf{x}, \lambda\dot{\mathbf{x}}) = \mathcal{F}(\mathbf{x}, \lambda\mathcal{L}_{\mathbf{x}}\dot{\mathbf{x}}) = \lambda\mathcal{F}(\mathbf{x}, \mathcal{L}_{\mathbf{x}}\dot{\mathbf{x}}) = \lambda\mathfrak{F}(\mathbf{x}, \dot{\mathbf{x}})$ and that $\mathfrak{F}(\mathbf{x}, \mathbf{0}) = \mathcal{F}(\mathbf{x}, \mathbf{0}) = 0$, by linearity of $\mathcal{L}_{\mathbf{x}}$, we obtain as announced that $\mathfrak{F}$ is a metric. Finally, the announced expression of the Hamiltonian $\mathfrak{H}$ follows from the computation

$$\max_{\dot{\mathbf{x}} \in \mathfrak{B}(\mathbf{x})} \langle \hat{\mathbf{x}}, \dot{\mathbf{x}} \rangle = \max_{\dot{\mathbf{x}} \in \mathcal{B}(\mathbf{x})} \langle \hat{\mathbf{x}}, \mathcal{L}_{\mathbf{x}}^{-1}\dot{\mathbf{x}} \rangle = \max_{\dot{\mathbf{x}} \in \mathcal{B}(\mathbf{x})} \langle \mathcal{L}_{\mathbf{x}}^{-\top}\hat{\mathbf{x}}, \dot{\mathbf{x}} \rangle,$$

which concludes the proof. $\square$

Proposition 3.2 *The considered variant of the classical elastica model, equipped with a continuous curvature prior map $\omega : \mathbb{M} \to \mathbb{R}$, defines a metric with explicit expression in Eq. (17), with control sets*

$$\mathfrak{B}(\mathbf{x}) := \Big\{ \dot{\mathbf{x}} = (\dot{x}, \dot{\theta}) \in \mathbb{E} \mid \dot{x} = \dot{\mathrm{n}}(\theta)\|\dot{x}\|, \\ \left(\|\dot{x}\| - \tfrac{1}{2}\right)^2 + \beta^2 \left(\dot{\theta} - \omega(\mathbf{x})\|\dot{x}\|\right)^2 \leq \tfrac{1}{4} \Big\}, \quad (18)$$

for all $\mathbf{x} = (x, \theta) \in \mathbb{M}$, and whose Hamiltonian reads

$$\mathfrak{H}(\mathbf{x}, \hat{\mathbf{x}}) = \\ \frac{1}{8} \left(\langle \hat{\mathbf{x}}, \dot{\mathrm{n}}(\theta, \omega(\mathbf{x})) \rangle + \sqrt{\langle \hat{\mathbf{x}}, \dot{\mathrm{n}}(\theta, \omega(\mathbf{x})) \rangle^2 + (\hat{\theta}/\beta)^2} \right)^2,$$

for all co-vectors $\hat{\mathbf{x}} = (\hat{x}, \hat{\theta}) \in \mathbb{E}^*$. Recall that $\dot{\mathrm{n}}(\theta, a) := ((\cos\theta, \sin\theta), a) \in \mathbb{E} := \mathbb{R}^2 \times \mathbb{R}$. This Hamiltonian can also be written as:

$$\mathfrak{H}(\mathbf{x}, \hat{\mathbf{x}}) = \frac{3}{8} \int_{-\pi/2}^{\pi/2} \langle \hat{\mathbf{x}}, \dot{\mathrm{q}}(\mathbf{x}, \varphi) \rangle_+^2 \cos\varphi d\varphi, \qquad (19)$$

where $\dot{\mathrm{q}}(\mathbf{x}, \varphi) \in \mathbb{E}$ is defined for any $\varphi \in [-\pi/2, \pi/2]$ as

$$\dot{\mathrm{q}}(\mathbf{x}, \varphi) := \left(\dot{\mathrm{n}}(\theta)\cos\varphi, \omega(\mathbf{x})\cos\varphi + \beta^{-1}\sin\varphi\right).$$

Proof Let us fix $\mathbf{x} = (x, \theta) \in \mathbb{M}$ in the following. Consider the linear map $\mathcal{L}_{\mathbf{x}} : \mathbb{E} \to \mathbb{E}$ defined for all $\dot{\mathbf{x}} = (\dot{x}, \dot{\theta}) \in \mathbb{E}$ as

$$\mathcal{L}_{\mathbf{x}}(\dot{\mathbf{x}}) := (\dot{x}, \dot{\theta} - \omega(\mathbf{x})\langle\dot{\mathrm{n}}(\theta), \dot{x}\rangle).$$

For clarity, let us also provide the matrix of this operator in the canonical basis of the three-dimensional space $\mathbb{E} = \mathbb{R}^2 \times \mathbb{R}$

$$[\mathcal{L}_{\mathbf{x}}] = \begin{pmatrix} 1 & 0 & -\omega(\mathbf{x})\cos\theta \\ 0 & 1 & -\omega(\mathbf{x})\sin\theta \\ 0 & 0 & 1 \end{pmatrix}. \qquad (20)$$

Then $\mathcal{L}_{\mathbf{x}}$ depends continuously on the point $\mathbf{x}$, and is invertible in view of the triangular form of its matrix. Since $\mathfrak{F}(\mathbf{x}, \dot{\mathbf{x}}) =$
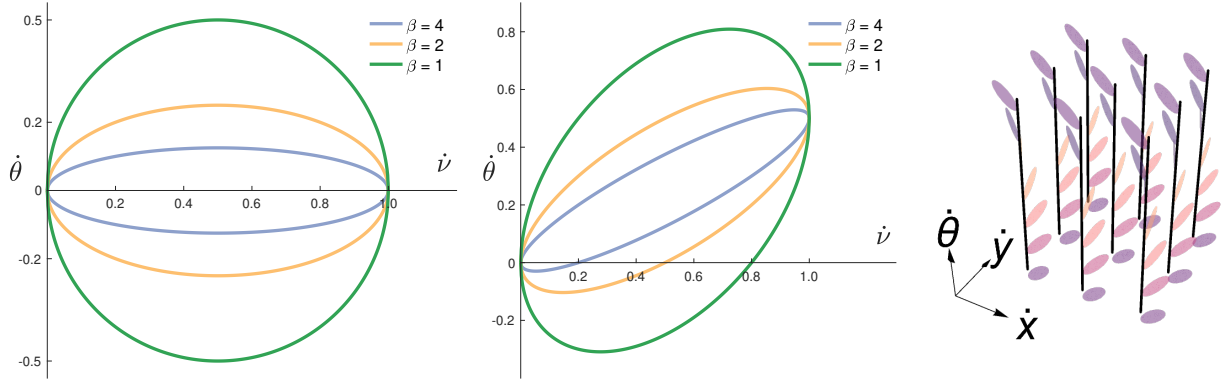
Fig. 3 Illustration of the control sets associated with the classical elastica model and the curvature prior elastica model. **Left**: The lines of different colors denote the sets of all $(\dot{\nu}, \dot{\theta})$ such that $\mathcal{F}(\mathbf{x}, (\dot{\nu}\dot{\mathrm{n}}(\theta), \dot{\theta})) = 1$ w.r.t. curvature penalization parameter $\beta \in \{1, 2, 4\}$, where $\dot{\nu} := \|\dot{x}\|$. Each of these sets is the boundary of the intersection between the control set $\mathcal{B}(\mathbf{x})$ of the elastica metric $\mathcal{F}$ and the slice defined by $\dot{x} = \dot{\mathrm{n}}(\theta)\|\dot{x}\|$. **Center**: Likewise for the curvature prior elastica model with $\omega(\mathbf{x}) = 1/2$. **Right**: Control sets for the curvature prior elastica model, embedded in the tangent space $\mathbb{E} = \mathbb{R}^2 \times \mathbb{R}$.

$\mathcal{F}(\mathbf{x}, \mathcal{L}_{\mathbf{x}}\dot{\mathbf{x}})$, indeed compare Eq. (17) with Eq. (5), the variant of the elastica model equipped with the curvature prior ω defines a valid metric whose control sets and Hamiltonian can be expressed in terms of those of the classical Euler-Mumford elastica model, see Theorem 3.1. More precisely, noting the equivalence $\dot{\mathbf{x}} \in \mathfrak{B}(\mathbf{x}) \Leftrightarrow \mathcal{L}_{\mathbf{x}}\dot{\mathbf{x}} \in \mathcal{B}(\mathbf{x})$ and using the characterization of $\mathcal{B}(\mathbf{x})$ established in Eq. (8), we obtain Eq. (18). From Eq. (20), we can easily compute the inverse and the transposed inverse mappings, namely

$$\mathcal{L}_{\mathbf{x}}^{-1}(\dot{\mathbf{x}}) = (\dot{x}, \dot{\theta} + \omega(\mathbf{x})\langle\dot{\mathrm{n}}(\theta), \dot{x}\rangle), \quad \forall \dot{\mathbf{x}} = (\dot{x}, \dot{\theta}) \in \mathbb{E},$$

$$\mathcal{L}_{\mathbf{x}}^{-\top}(\hat{\mathbf{x}}) = (\hat{x} + \omega(\mathbf{x})\dot{\mathrm{n}}(\theta), \hat{\theta}), \quad \forall \hat{\mathbf{x}} = (\hat{x}, \hat{\theta}) \in \mathbb{E}^*.$$

Note that

$$\langle\mathcal{L}_{\mathbf{x}}^{-\top}\hat{\mathbf{x}}, \dot{\mathrm{n}}(\theta, 0)\rangle = \langle\hat{\mathbf{x}}, \mathcal{L}_{\mathbf{x}}^{-1}\dot{\mathrm{n}}(\theta, 0)\rangle = \langle\hat{\mathbf{x}}, \dot{\mathrm{n}}(\theta, \omega(\mathbf{x}))\rangle$$

and likewise that

$$\langle\mathcal{L}_{\mathbf{x}}^{-\top}\hat{\mathbf{x}}, (\dot{\mathrm{n}}(\theta)\cos\varphi, \beta^{-1}\sin\varphi)\rangle = \langle\hat{\mathbf{x}}, \dot{\mathrm{q}}(\mathbf{x}, \varphi)\rangle.$$

Evaluating Eq. (9) and Eq. (10) at $\mathcal{L}_{\mathbf{x}}^{-\top}(\hat{\mathbf{x}})$, and using the previous identities, we obtain the announced expressions of the Hamiltonian $\mathfrak{H}$, which concludes the proof.

The integral form of the Hamiltonian $\mathfrak{H}$, formulated in Eq. (19) can be approximated using the L-point Fejer quadrature rule for any positive integer L, following (Mirebeau, 2018). This yields

$$\mathfrak{H}(\mathbf{x}, \hat{\mathbf{x}}) = \sum_{l=1}^{L} \mu_l \langle\hat{\mathbf{x}}, \dot{\mathrm{q}}(\mathbf{x}, \varphi_l)\rangle_+^2 + \|\hat{\mathbf{x}}\|^2 \mathcal{O}(L^{-2}), \qquad (21)$$

where we denoted by $\mu_l > 0$ the weights of the Fejer quadrature rule at the angles $\varphi_l = (2l - 1 - L)\pi/(2L) \in [-\pi/2, \pi/2]$, for any $1 \le l \le L$. This approximation plays a crucial role in the HFM method, as presented in next section.

4 Application to Tracking Curvilinear Structures

Geodesic paths are considered as a powerful tool for interactive curvilinear structure tracking (Cohen and Kimmel, 1997; Li and Yezzi, 2007; Péchaud et al, 2009; Liao et al, 2018; Chen et al, 2019). Following the spirit of this line of works, we propose a fast and reliable method for computing a curvature

prior map ω from image data, allowing the curvature prior elastica model to accurately extract curvilinear structures of interest. This computation method, presented in the remainder of this section, consists of two main steps: (I) the generation of a set of disjoint curvilinear structure centerlines, and (II) the estimation of the tangent direction and curvature associated with those disjoint centerlines.

4.1 Generation of the Disjoint Centerlines

Centerlines serve as an effective descriptor for curvilinear structures, by which geometric features such as their tangent direction and curvature properties can be estimated. A broad variety of approaches have been introduced to handle the task of extracting centerlines from curvilinear structure networks which usually include complex junctions, e.g. (Kaul et al, 2012; Cetin et al, 2012; Türetken et al, 2016). Among those methods, the skeletonization schemes, adopted in this work, provide a powerful way for producing centerlines as the skeletons of the pre-segmented curvilinear structures (Kimmel et al, 1995; Siddiqi et al, 2002; Lam et al, 1992).

Let $\Xi : \Omega \to \{0, 1\}$ represent the binary segmentation of curvilinear structures contained in an image, where $\Xi(x) = 1$ implies that the position x belongs to a curvilinear structure, while $\Xi(x) = 0$ indicates a background position x. We compute the skeleton or medial axis of the elongated shapes $\{x \in \Omega \mid \Xi(x) = 1\}$, and remove all the junction points of these skeleton structures, yielding J disjoint skeleton segments, where J is a positive integer. After applying a curve smoothing procedure to regularize these skeleton segments, we obtain a family of smooth curves $\rho_j : [0, 1] \to \Omega$, indexed by $1 \le j \le J$, as the parametrization of the regularized skeleton segments. In what follows we refer to these curves ρ_j as *candidate centerlines*.

In practice, we rely on morphological filters (Lam et al, 1992), which benefit from a low computational complexity, to generate skeletons from pre-segmentation data. Fig. 4 illustrates an example for constructing the candidate centerlines $\{\rho_j\}_{1 \le j \le J}$ using a synthetic image. Fig. 4b visualizes the corresponding binary segmentation map Ξ. In Fig. 4c, the candidate centerlines are illustrated using different colors, and arrows indicate their directions. The curvature of these candidate centerlines is depicted in Fig. 4d.
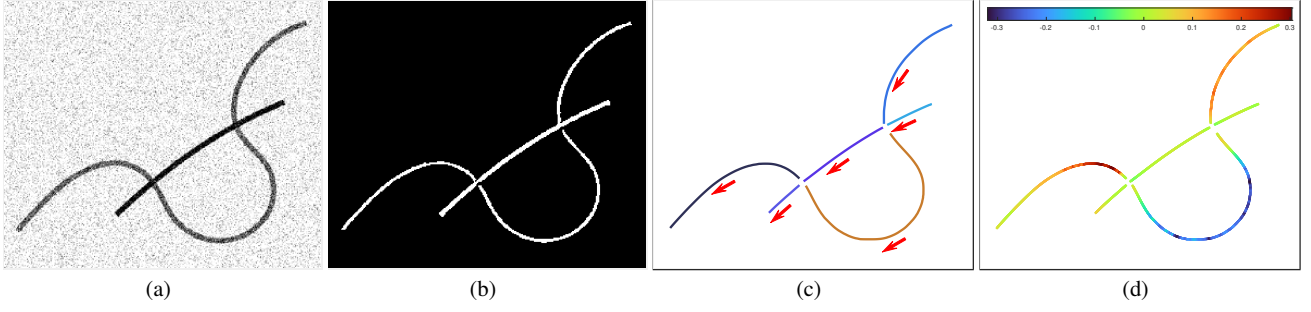
Fig. 4 An example for the construction of candidate centerlines. **a** The original image. **b** Visualizing the binary segmentation map Ξ. **c** The candidate centerlines ρ_j indicated by different colors. The arrows illustrate the directions of the corresponding candidate centerlines. **d** Visualizing the curvature of the candidate centerlines.

Note that a curvilinear structure of interest usually corresponds to the concatenation of several candidate centerlines, together with the crucial curves connecting pairs of adjacent centerlines. For this reason, the skeletonization process is not an appropriate solution to the curvilinear structure tracking problem considered, but rather an efficient descriptor for extracting the geometric features of parts of the curvilinear structures.

4.2 Construction of the Curvature Prior Map ω

We propose to estimate the curvature prior map ω using the computed candidate centerlines ρ_j, whose curvature and unit normal are respectively denoted by $\kappa_j : [0,1] \to]-\infty, \infty[$ and $\mathcal{N}_j : [0,1] \to \mathbb{R}^2$, for $1 \leq j \leq J$.

Let $0 < U < \min_j\{1/\|\kappa_j\|_\infty\}$ be a bounded constant. Consider the mapping $\Psi_j : [0,1] \times [-U, U] \to \mathbb{R}^2$, depending on the curve parameter and the deviation from ρ_j, defined as

$$\Psi_j(u, \lambda) := \rho_j(u) + \lambda \mathcal{N}_j(u)$$

for any $u \in [0,1]$ and $\lambda \in [-U, U]$. The bounding constraint on the parameter U implies that the mappings Ψ_j are injective, and each of them parametrizes a tubular neighborhood $\mathfrak{T}_j \subset \Omega$ of width U surrounding the candidate centerline ρ_j

$$\mathfrak{T}_j := \{x = \Psi_j(u, \lambda) \in \Omega \mid \forall u \in [0,1] \text{ and } \forall \lambda \in [-U, U]\}.$$

However, such a tubular neighborhood $\mathfrak{T}_i$ may intersect with a distinct one $\mathfrak{T}_j$, i.e. $\mathfrak{T}_i \cap \mathfrak{T}_j \neq \emptyset$, when their centerlines ρ_i and ρ_j are close to each other. In order to tackle this problem, we partition the domain Ω into a series of disjoint regions $\mathcal{V}_j \subset \Omega$ for $1 \leq j \leq J$

$$\mathcal{V}_j := \left\{ x \in \Omega \mid d_{\rho_j}(x) < d_{\rho_i}(x), \ \forall i \neq j \right\}, \tag{22}$$

where $d_{\rho_j}(x)$ denotes the Euclidean distance between x and the candidate centerline ρ_j. These regions are also known as the Voronoi cells. Accordingly, for each ρ_j a modified tubular neighborhood $\mathcal{T}_j \subset \Omega$ can be constructed by

$$\mathcal{T}_j := \mathfrak{T}_j \cap \mathcal{V}_j, \tag{23}$$

which satisfies $\mathcal{T}_j \cap \mathcal{T}_i = \emptyset$ for any $i \neq j$. In practice, the construction of the Voronoi cells $\mathcal{V}_j$ can be efficiently implemented by propagating an unsigned Euclidean distance map simultaneously from all the candidate centerlines Saye and Sethian (2011, 2012).

We consider two scalar-valued functions $\phi : \cup_j \mathcal{T}_j \to \mathbb{R}$ and $\vartheta : \cup_j \mathcal{T}_j \to \mathbb{S}^1$ using all the candidate centerlines ρ_j, $1 \leq j \leq J$, such that for any physical position $x = \Psi_j(u, \lambda) \in \mathcal{T}_j$, one respectively has

$$\phi(x) := \kappa_j(u), \text{ and } \dot{\mathrm{n}}(\vartheta(x))\|\rho'_j(u)\| = \rho'_j(u).$$

The function ϕ extends the curvature of the candidate centerlines ρ_j to their respective neighborhood regions $\mathcal{T}_j$ of width U. Furthermore, for a physical position $x \in \mathcal{T}_j$, the angles $\vartheta(x)$ and $\vartheta(x) + \pi$ correspond to the two possible orientations that the elongated structure should have at the position x. With these definitions, the curvature prior map ω can be generated in terms of the estimated functions ϕ and ϑ. More precisely, we define the curvature prior map ω for any point $\mathbf{x} = (x, \theta) \in \mathbb{M}$ as follows

$$\omega(\mathbf{x}) := \begin{cases} \phi(x)\,\mathrm{sign}\left(\langle \dot{\mathrm{n}}(\theta), \dot{\mathrm{n}}(\vartheta(x))\rangle\right), & \forall \mathbf{x} \in \cup_j \mathcal{T}_j \times \mathbb{S}^1, \\ 0, & \text{otherwise,} \end{cases} \tag{24}$$

where $\mathrm{sign}(a)$ stands for the sign of a scalar value $a \in \mathbb{R}$. In the first line of Eq. (24), for any physical position $x \in \cup_j \mathcal{T}_j$ we set $\omega(x, \theta) = \omega(x, \vartheta(x)) = \phi(x)$ if the angular position θ is closer to $\vartheta(x)$ in the sense of the Euclidean scalar product of the vectors $\dot{\mathrm{n}}(\theta)$ and $\dot{\mathrm{n}}(\vartheta(x))$, and $\omega(x, \theta) = \omega(x, \vartheta(x) + \pi) = -\phi(x)$ if θ is closer to $\vartheta(x) + \pi$.

4.3 Computation of the Cost Function ψ

The multi-orientation data-driven cost function $\psi(x, \theta)$ should have low values when both (i) the physical position x is close to the centerline of a curvilinear structure, and (ii) the direction $\dot{\mathrm{n}}(\theta)$ closely aligns with the tangent of this centerline at the physical position x. For that purpose and following (Chen et al, 2017; Duits et al, 2018; Bekkers et al, 2015a), we build the cost function ψ for any point $\mathbf{x} = (x, \theta) \in \mathbb{M}$ as follows

$$\psi(\mathbf{x}) = \exp\left(-\alpha \frac{g(\mathbf{x})}{\|g\|_\infty}\right), \tag{25}$$

where $\alpha > 0$ is a positive weighting parameter, and where $g : \mathbb{M} \to [0, \infty[$ is an orientation score map usually taken as an efficient tool in image analysis (Franken and Duits, 2009; Hummel and Zucker, 1983; Bekkers et al, 2014; Parent and Zucker, 1989). This map carries the curvilinear appearance and anisotropy features, and obeys $g(x, \theta) = g(x, \theta + \pi)$,
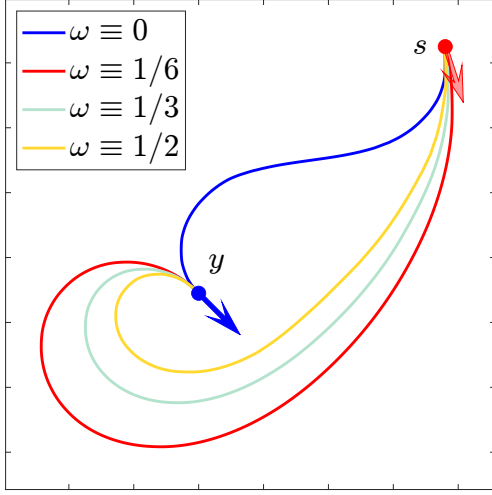
Fig. 5 Illustration of the physical projections of geodesic paths for the curvature prior elastica model with different values of ω. The red and blue dots with the associated arrows represent the source and target points of the geodesic paths, respectively.

$\forall (x, \theta) \in \mathbb{M}$. In this work, the steerable optimally oriented flux filter (Law and Chung, 2008) is chosen as the curvilinear feature extractor in order to compute the orientation score g. We refer to (Chen et al, 2017) for more details on the computation of the orientation score map g from image data involving curvilinear structures.

4.4 Initialization and Geodesic Paths Tracking

The curvilinear structure tracking method can be implemented in an interactive manner, requiring a source point $\mathbf{s} = (s, \theta_s) \in \mathbb{M}$ and a target point $\mathbf{y} = (y, \theta_y) \in \mathbb{M}$ as initialization. In our model, we assume that the physical positions s and y are provided by the user. Furthermore, the corresponding angles θ_s and θ_y can be either given by the user in complex scenarios, or be estimated from the cost function ψ as

$$\theta_s = \underset{\theta \in [0, \pi[}{\arg\min} \, \psi(s, \theta). \tag{26}$$

In addition to the points $\mathbf{s}$ and $\mathbf{y}$ as described above, we generate another pair of source and target points $\tilde{\mathbf{s}} = (s, \theta_s + \pi)$ and $\tilde{\mathbf{y}} = (y, \theta_y + \pi)$. In other words, $\mathbf{s}$ and $\tilde{\mathbf{s}}$ (resp. $\mathbf{y}$ and $\tilde{\mathbf{y}}$) share the same physical position but different angular positions. In this case, the goal is to find a minimal geodesic path from the source point set $\mathfrak{s} = \{\mathbf{s}, \tilde{\mathbf{s}}\}$ to the target point set $\mathfrak{y} = \{\mathbf{y}, \tilde{\mathbf{y}}\}$, as considered in (Chen et al, 2017). For that purpose, a geodesic distance map $\mathcal{D}_{\mathfrak{s}}$ is estimated by solving the HJB PDE

$$\mathfrak{H}(\mathbf{x}, d\mathcal{D}_{\mathfrak{s}}(\mathbf{x})) = \frac{1}{2} \psi(\mathbf{x})^2,$$

for all $\mathbf{x} \in \mathbb{M} \setminus \mathfrak{s}$, with the boundary condition $\mathcal{D}_{\mathfrak{s}}(\mathbf{x}) = 0$ for any point $\mathbf{x} \in \mathfrak{s}$, which is a straightforward generalization of the single source case described in Eq. (28). The geodesic of interest is backtracked, as described in Eq. (13), from the point of the target set $\mathfrak{y}$ whose geodesic distance value is smallest, and by the nature of the viscosity solution the backtracking procedure ends at the point of the seed set $\mathfrak{s}$ which is closest w.r.t. the metric. For computational efficiency, the
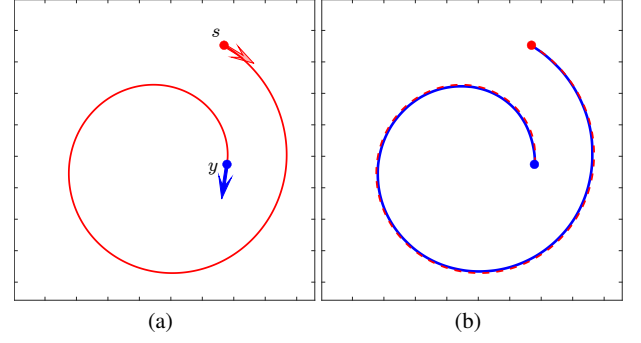

Fig. 6 Illustration of the extraction of a smooth curve using the curvature prior elastica model. **a** A smooth planar curve whose endpoints s and y are respectively denoted by the red and blue dots. The arrows represent the tangent vectors at the endpoints s and y of the planar curve. **b** The blue solid line denotes the physical projection of the geodesic path from the curvature prior elastica model, and the red dashed line illustrates the given smooth curve.

procedure for estimating the respective geodesic distances can be terminated immediately once either point of the target set $\mathfrak{y}$ is reached by the fast marching front, and this optimization is valid since the fast marching front advances monotonically. Note that this geodesic path tracking procedure allows the user *not* to distinguish between the source and target points, which is convenient in practice.

5 Experimental Results

In this section, we present numerical results obtained with the introduced curvature prior elastica model. Our experiments are meant to illustrate the influence of the curvature prior term ω, and for that purpose we perform qualitative and quantitative comparisons with the classical elastica model (Chen et al, 2017; Mirebeau, 2018), on curvilinear structure tracking tasks applied to both synthetic and real images. In the remainder of this section, both geodesic models are configured using the identical setting, except for the curvature prior term which is set to $\omega \equiv 0$ for the classical elastica model.

Fig. 5 illustrates several geodesic paths from the curvature prior elastica geodesic model where the term ω is set as a *constant function* with different values. The cost function is set as $\psi \equiv 1$. The orientation-lifted source point $\mathbf{s} = (s, \theta_s) \in \mathbb{M}$ is shown as a red dot at the position s equipped with an arrow pointing in the direction $\dot{\mathrm{n}}(\theta_s)$, and likewise for the target point $\mathbf{y} = (y, \theta_y)$ in blue. In this figure, the planar physical projections of four distinct geodesic paths corresponding to different values of ω are illustrated. The blue line corresponds to the geodesic path from the classical elastica model (i.e. $\omega \equiv 0$). As the value of ω increases, we observe in this figure that the portions of these geodesic paths surrounding the target point feature turns with diminishing turning radius.

Fig. 6 illustrates a geodesic path computed using the curvature prior elastica model, where the curvature prior term $\omega : \mathbb{M} \to \mathbb{R}$ is estimated pointwise from a given smooth curve as described in Eq. (24), and the cost function $\psi \equiv 1$ is constant. The given reference curve is shown on Fig. 6a, and connects an endpoint s to another one y, with tangent directions $\dot{\mathrm{n}}(\theta_s)$ and $\dot{\mathrm{n}}(\theta_y)$ shown as red and blue arrows respectively. The blue solid line in Fig. 6b illustrates the
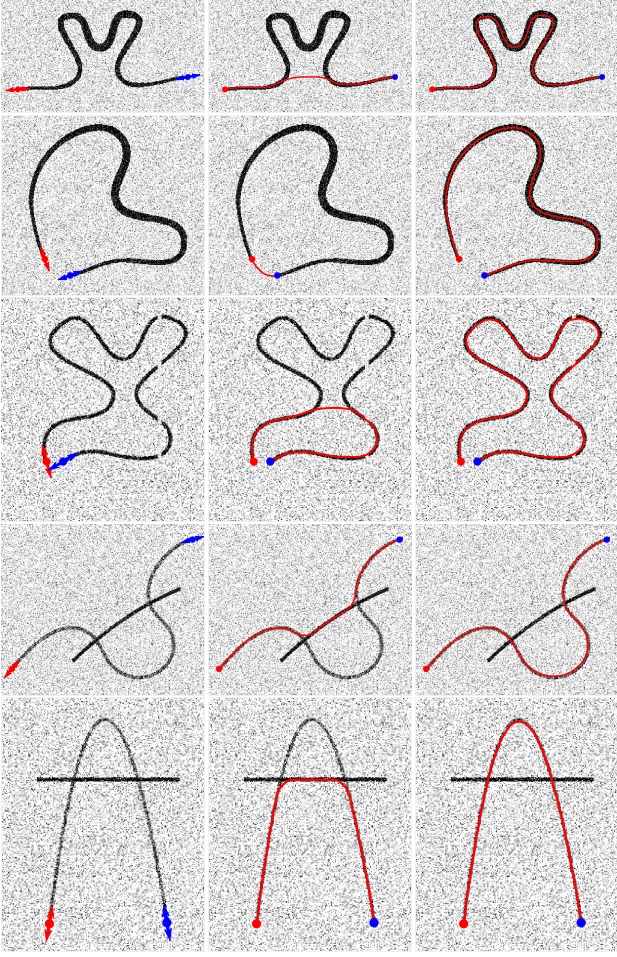
Fig. 7 Qualitative comparison results on synthetic images blurred by additive Gaussian noise. The initialization for each image is shown in column 1, where the red and blue dots with the respective arrows indicate the source and target points. The physical projections of the geodesic paths from the classical elastica model and the curvature prior elastica model are respectively illustrated with red lines in columns 2 and 3.

Fig. 8 Qualitative comparison results on retinal images. **Left**: The initialization. The blue and red dots with the associated arrows indicate the source and target points. **Center** and **Right**: The computed minimal geodesic paths (red lines) for the classical elastica model and the curvature prior elastica model, respectively.

physical projection of the geodesic path obtained using the variant of the elastica model, equipped with the estimated curvature prior map ω described above, from the source point $\mathbf{s} = (s, \theta_s)$ to the target point $\mathbf{y} = (y, \theta_y)$. In Fig. 6b, the reference smooth curve is shown in red and dashed. When the curvature penalization parameter β is sufficiently large, as in this experiment where we use $\beta = 20$, the physical projection of the computed geodesic path should be almost overlaid onto the reference smooth curve, since they have almost identical curvature (recall that by construction the energy functional penalizes the square of their curvature difference), and since they share their endpoints and tangents at these endpoints. More precisely, the physical projection of the computed geodesic path converges to the reference curve as $\beta \to \infty$, and to a straight line joining the endpoints as $\beta \to 0$. The computed geodesic path shown in Fig. 6b indeed well approximates the given reference curve, illustrating the effectiveness of the curvature prior in the considered variant of the classical elastica model.

5.1 Qualitative Comparison

In Fig. 7, we compare results obtained with the classical elastica model, and with the curvature prior elastica model, on
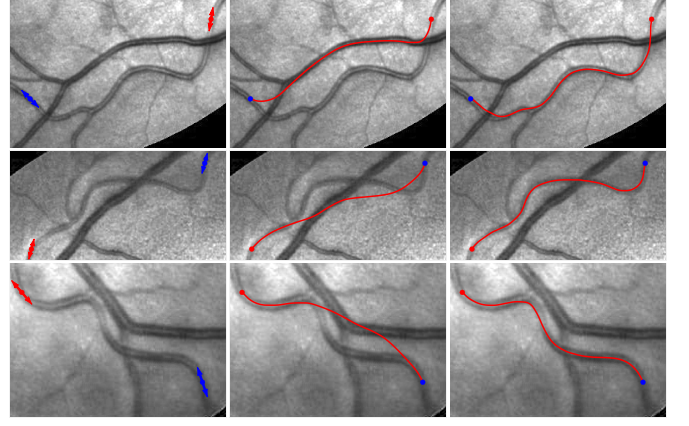
five synthetic images. A common feature for the curvilinear structures in those images is that each of them involves strongly bent segments. The first column of Fig. 7 shows the initialization information for each synthetic image, where the blue and red dots together with the arrows stand for the source and target points respectively used to define the sets $\mathfrak{s}$ and $\mathfrak{y}$. Columns 2 and 3 illustrate the physical projections of the computed geodesic paths from the classical elastica model and the curvature prior elastica model, respectively. More specifically, in column 2 of rows 1 to 3, we can observe that the physical projections of the geodesic paths from the classical elastica model are trapped into a shortcut problem, i.e. the projected paths travel along non-target regions. The reason is that the "correct" path features strongly curved segments whose squared curvature accumulate and lead to a high value of the classical elastica energy, hence it is not selected by this model. In contrast, in column 3 of the same rows, the curvature prior elastica model indeed leads to accurate extraction of the target structures, even through the two endpoints of the structures in rows 2 and 3 are very close to each other. In rows 4 and 5, each of the curvilinear structures is interrupted by an almost straight segment with slightly stronger appearance features, i.e. with higher values of the orientation score along this segment, yielding challenging crossing structures. In these tests, the physical projections of the geodesic paths from the classical elastica model pass through the interrupting segments, yielding a short branches combination problem (Chen et al, 2018), i.e. the obtained geodesic paths travel different segments not belonging to the targets. In contrast, the curvature prior elastica model produces satisfactory results which are able to accurately delineate the target curvilinear structures, as shown in column 3.

Fundus vessel tracking is a task of fundamental importance in retinal imaging and the relevant disease diagnosis. In Fig. 8, we compare the curvature prior elastica model to the classical elastica model in 3 patches of retinal fundus images, chosen from the IOSTAR dataset (Zhang et al, 2016). In this experiment, the goal is to extract artery blood vessels, given two endpoints of each target vessel, as shown in the left column of Fig. 8. In a typical retinal fundus image, the major artery vessels usually exhibit weaker appearance features than

Fig. 9 Qualitative comparison results on road images. **Left**: The initialization. The red and cyan dots with the respective arrows indicate the source and target points. **Center** and **Right**: The computed minimal geodesic paths (red lines) for the classical elastica model and the curvature prior elastica model, respectively.

Table 1 Quantitive comparison between the classical Euler-Mumford elastica model and the curvature prior elastica model on synthetic images, illustrated by the average and the standard deviation of the Jaccard score values.

	Elastica Model		Curvature Prior Elastica Model	
	Ave.	Std.	Ave.	Std.
$\beta = 4.5$	52.72%	0.27	91.83%	0.03
$\beta = 6.0$	51.47%	0.26	90.61%	0.07

those of the nearby vein vessels, and often cross over vein vessels yielding junction structures. An additional difficulty is that the target artery vessels also consist of segments with strong tortuosity. For the classical Euler-Mumford elastica model, one needs to assign a low importance weight to the curvature term, in order to avoid the underlying shortcut problem at those segments. However, this in turn encourages the computed paths to pass through the stronger neighboring vein vessels (whose cost ψ is lower), thus increasing the risk of the short branches combination problem, see the center column of Fig. 8. In contrast, the minimization of the energy (16) defining the curvature prior elastica model favors optimal geodesic paths whose curvature is close to ω, allowing to handle scenarios where challenging structures such as crossings and strongly bent segments appear, see the right column of Fig. 8.

Another practical application for geodesic models is road tracking from aerial images, as demonstrated in Fig. 9. In this experiment, the centerlines of the objective roads have high Euclidean length, and simultaneously feature segments with low turning radii, as shown in Fig. 9a. We can see that the classical elastica model generates tracking results which suffer from a shortcut problem, see the center column of Fig. 9. In contrast, accurate results derived from the curvature prior elastica model are observed in the right column of Fig. 9, thanks to the use of the curvature prior term which alleviates difficulties associated to the complex scenarios.

5.2 Quantitative Comparison

We perform a quantitative evaluation of the performance and stability of the classical elastica model and of the curvature

prior elastica model on synthetic images, when one varies the parameters β and α involved in these models, see Eqs. (16) and (25). These parameters determine the balance between the image data and the curvature regularization. The test data are generated by incorporating different levels of additive Gaussian noise to the original binary images of those shown in Fig. 7. More specifically, we add zero-mean Gaussian noise with 16 levels of normalized variance values between 0 and 0.15 to each clean image, producing $16 \times 5 = 80$ test images. Both geodesic models are configured by choosing parameters $\beta \in \{4.5, 6\}$ and $\alpha \in \{3, 4, 5\}$, thus yielding 6 runs per test image. In each test, the accuracy of the curvilinear structure tracking is measured using the Jaccard score between two bounded regions $A, B \subset \mathbb{R}^2$, defined as

$$\mathrm{JS}(A, B) := \frac{|A \cap B|}{|A \cup B|}, \tag{27}$$

where $|A|$ represents the area of the region A. In our case, the regions A and B are defined as tubular neighborhoods with a fixed radius of 6 grid points along the ground truth centerline and the physical projection of the computed geodesic path, respectively. Table 1 shows the quantitative results comparing the classical elastica model and the curvature prior elastica model, in terms of the Jaccard score between the ground truth centerlines and the physical projections of geodesic paths, see (27). In each row of Table 1, the average (Ave.) and standard deviation (Std.) values of JS, which are derived from 480 runs w.r.t. different values of the parameters α and β. Overall, the results from the classical Euler-Mumford elastica model in general exhibit low average values of JS, and large standard deviation, reflecting the fact that various shortcut and short branches combination problems occur in most of the tests. In contrast, we observe much higher average values of JS using the curvature prior elastica model, and a smaller standard deviation, illustrating its ability to accurately and robustly extract curvilinear structures in the presence of strongly bent segments and junctions.

6 Conclusion and Discussion

In this work, we present a nonlinear HJB PDE approach to numerically compute the curve which globally minimizes a variant of the classical Euler-Mumford elastica energy, involving a curvature prior enhancement. The main contributions include (i) the establishment of the explicit expression of the Hamiltonian of the curvature prior elastica model, in such way that globally optimal paths can be characterized using the HJB PDE framework, (ii) the design of a finite differences scheme based on the HFM method for estimating the numerical solution to the associated HJB PDE, and (iii) the introduction of an efficient and robust method for computing the curvature prior in the context of curvilinear structure tracking. Numerical experiments indeed demonstrate promising results in medical and aerial images.

From the modeling standpoint, rather than penalizing the difference to a given curvature prior ω as proposed here, an alternative interesting route would be to penalize the variation of curvature along the path. The latter approach indeed appears to be appropriate and reasonable in relevant applications; for instance it would naturally address the shortcut problem, a

segmentation artefact which usually involves sharp turns. For that purpose, one may for instance introduce in the elastica energy defined in (15) the squared derivative $\kappa'(\cdot)^2$ of the path curvature. However, this defines a third-order geodesic model, which raises substantial numerical difficulties. A closely related problem considered in the literature is the computation of geodesic paths with bounded derivative of curvature, however the approach Bakolas and Tsiotras (2009) cannot take into account a data-driven cost function, which is required by image processing applications. Another related problem is the penalization of torsion, a quantity which is also defined in terms of the third-order derivatives of the path, and is approximated in Ulen et al (2015) with the torsion of some local Bezier interpolations of the path. In the HJB PDE framework, considered in this paper, the computation of minimal geodesic paths for third-order planar models as considered here would involve the numerical solution of a strongly anisotropic PDE posed on the four dimensional domain $\Omega \times \mathbb{S}^1 \times \mathbb{R} \ni (\mathbf{x}, \theta, \kappa)$, which implies an increased computational cost. We regard it as an opportunity for future research.

We have introduced a practical method for computing the curvature prior ω, using a set of reconstructed piecewise smooth centerlines which reflect the geometry of curvilinear structures in the image. In our work, those centerlines are numerically generated by applying a skeletonization procedure on the segmented curvilinear structures. A proper integration of the voting method Rouchdy and Cohen (2013) and of the keypoints detection method Benmansour and Cohen (2009); Kaul et al (2012) might be an alternative way for constructing the centerlines, where the dependency on the segmentation process can be removed. Furthermore, the estimation of the curvature of curves or surfaces from an orientation score map could also be investigated for computing ω, e.g. Bekkers et al (2015b). Unfortunately, the orientation score values around the positions where complex junctions appear usually lack reliability, thus requiring additional procedures to alleviate this problem.

We have established in Theorem 3.1 a general theoretical framework for deriving the Hamiltonian and control set of a curvature-penalized geodesic model equipped with a curvature prior enhancement, and have shown its application to the Euler-Mumford elastica model. This framework can also be exploited to generalize the Reeds-Sheep forward model Duits et al (2018) and the Dubins car model Mirebeau (2018). Finally, we intend to use the curvature-penalized geodesic models with curvature prior enhancement to address various image segmentation problems.

Appendix A Finite Difference Scheme for the Hamiltonian $\mathfrak{H}$

We introduce here the numerical scheme for estimating the geodesic distance map associated to the Hamiltonian $\mathfrak{H}$ based on the state-of-the-art HFM method Mirebeau (2018, 2019). Recall that the distance map $\mathcal{D}_{\mathbf{s}}$ is the unique viscosity solution to the static HJB PDE

$$\mathfrak{H}(\mathbf{x}, d\mathcal{D}_{\mathbf{s}}(\mathbf{x})) = \tfrac{1}{2}\psi(\mathbf{x})^2, \quad \forall \mathbf{x} \in \mathbb{M}\backslash\{\mathbf{s}\}, \qquad (28)$$

with the same point source $\mathbf{s}$ and outflow boundary conditions as in (12). We discretize this PDE over the Cartesian grid

$$\mathbb{M}_h := (h\mathbb{Z}^2 \times (h\mathbb{Z}/2\pi\mathbb{Z})) \cap \mathbb{M},$$

where h is the grid scale, which is chosen so that $2\pi/h$ is a positive integer for periodicity. Note that $h\mathbb{Z}/2\pi\mathbb{Z} = \{0, h, \cdots, (N_\theta - 1)h\} \subset \mathbb{S}^1$, where $N_\theta := 2\pi/h$ represents the number of angles discretized in the orientation dimension. We fix $N_\theta = 72$ in the numerical experiments of this paper.

Given a non-zero vector $\dot{\mathbf{v}} \in \mathbb{E}$ and a relaxation parameter $\varepsilon \in]0, 1[$, a crucial ingredient of the HFM method Mirebeau (2018) is an approximation of the form

$$\langle \hat{\mathbf{x}}, \dot{\mathbf{v}} \rangle_+^2 = \sum_{k=1}^K \xi_k^\varepsilon(\dot{\mathbf{v}}) \langle \hat{\mathbf{x}}, \dot{\mathbf{e}}_k^\varepsilon(\dot{\mathbf{v}}) \rangle_+^2 + \|\hat{\mathbf{x}}\|^2 \|\dot{\mathbf{v}}\|^2 \mathcal{O}(\varepsilon^2), \quad (29)$$

for any co-vector $\hat{\mathbf{x}} \in \mathbb{E}^*$, where $\xi_k^\varepsilon(\dot{\mathbf{v}}) \geq 0$ is a non-negative weight, and $\dot{\mathbf{e}}_k^\varepsilon(\dot{\mathbf{v}}) \in \mathbb{Z}^3$ is an offset having integer coordinates, for each $1 \leq k \leq K$ where K is a positive integer. The construction of these weights and offsets relies on Selling's decomposition of positive quadratic forms Mirebeau (2014b), with $K = 6$ in dimension $\dim(\mathbb{E}) = 3$, and $\|\dot{\mathbf{e}}_k^\varepsilon(\dot{\mathbf{v}})\| = \mathcal{O}(\varepsilon^{-1})$. In practice, we use $\varepsilon = 0.1$.

By applying the approximation scheme in (29) to the terms of (21), we obtain the following expression

$$\langle \hat{\mathbf{x}}, \dot{\mathfrak{q}}(\mathbf{x}, \varphi_l) \rangle_+^2 \approx \sum_{k=1}^K \xi_k^\varepsilon(\dot{\mathfrak{q}}(\mathbf{x}, \varphi_l)) \langle \hat{\mathbf{x}}, \dot{\mathbf{e}}_k^\varepsilon(\dot{\mathfrak{q}}(\mathbf{x}, \varphi_l)) \rangle_+^2. \quad (30)$$

For the sake of readability, we leverage the abbreviations $\xi_{kl}^\varepsilon(\mathbf{x})$ and $\dot{\mathbf{e}}_{kl}^\varepsilon(\mathbf{x})$ to denote $\xi_k^\varepsilon(\dot{\mathfrak{q}}(\mathbf{x}, \varphi_l))$ and $\dot{\mathbf{e}}_k^\varepsilon(\dot{\mathfrak{q}}(\mathbf{x}, \varphi_l))$, respectively. Combining (21) with (30) yields the following approximation of the Hamiltonian $\mathfrak{H}$

$$\mathfrak{H}(\mathbf{x}, \hat{\mathbf{x}}) \approx \sum_{l=1}^L \mu_l \sum_{k=1}^K \xi_{kl}^\varepsilon(\mathbf{x}) \langle \hat{\mathbf{x}}, \dot{\mathbf{e}}_{kl}^\varepsilon(\mathbf{x}) \rangle_+^2. \quad (31)$$

The set $\mathcal{S}^\varepsilon(\mathbf{x}) = \{\dot{\mathbf{e}}_{kl}^\varepsilon(\mathbf{x})\}_{1 \leq l \leq L}^{1 \leq k \leq K} \subset \mathbb{Z}^3$ of all offsets, at a given discretization point $\mathbf{x} \in \mathbb{M}_h$, is known as the stencil of the HFM method and defines the neighborhood system of this numerical scheme, see Fig. 10.

Now we can discretize the introduced Hamiltonian $\mathfrak{H}$ using a first order upwind finite difference scheme Mirebeau (2018)

$$\langle d\mathcal{D}_{\mathbf{s}}(\mathbf{x}), \dot{\mathbf{e}} \rangle_+^2 = \left(\frac{\mathcal{D}_{\mathbf{s}}(\mathbf{x}) - \mathcal{D}_{\mathbf{s}}(\mathbf{x} - h\dot{\mathbf{e}})}{h} \right)_+^2 + \mathcal{O}(h), \quad (32)$$

for any discretization point $\mathbf{x} \in \mathbb{M}_h$ and any offset $\dot{\mathbf{e}} \in \mathcal{S}^\varepsilon(\mathbf{x})$. Since the offset $\dot{\mathbf{e}}$ has integer coordinates by construction, one has $\mathbf{x} - h\dot{\mathbf{e}} \in \mathbb{M}_h$, and therefore the r.h.s. of (32) only involves values of the unknown geodesic distance map $\mathcal{D}_{\mathbf{s}}$ on the discretization grid $\mathbb{M}_h$. Finally, we obtain a finite differences discrete counterpart of the HJB PDE defined in (28)

$$\sum_{l=1}^L \mu_l \sum_{k=1}^K \xi_{kl}^\varepsilon(\mathbf{x}) \left(\frac{\mathcal{D}_{\mathbf{s}}(\mathbf{x}) - \mathcal{D}_{\mathbf{s}}(\mathbf{x} - h\dot{\mathbf{e}}_{kl}^\varepsilon(\mathbf{x}))}{h} \right)_+^2 = \frac{1}{2}\psi(\mathbf{x})^2 \qquad (33)$$

for all $\mathbf{x} \in \mathbb{M}_h \backslash \{\mathbf{s}\}$, with boundary condition $\mathcal{D}_{\mathbf{s}}(\mathbf{s}) = 0$.

The HFM method computes the numerical solution to the discretized HJB PDE (see (33)) in an efficient single-pass

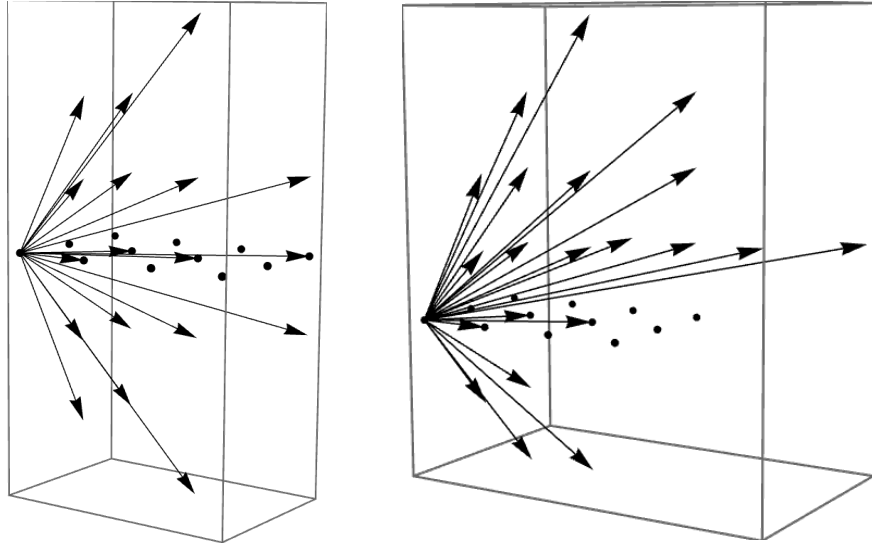**Fig. 10** Visualizing the stencils associated with the classical elastica model and the curvature prior elastica model. **Left**: Stencil $\mathcal{S}^{\varepsilon}(\mathbf{x})$ for the classical Euler-Mumford elastica model with $\beta = 2$, $\theta = \pi/6$, and discretization parameters $L = 5$, $\varepsilon = 0.1$. **Right**: Likewise for the curvature prior elastica model with $\omega(\mathbf{x}) = 0.5$. Note that the latter is not symmetric w.r.t. the horizontal plane.

wavefront propagation manner, using a generalization of the original Fast-Marching method Sethian (1999). Assuming that the computation is performed on a finite subset of the Cartesian grid $\mathbb{M}_h$, containing N_h points, the computation complexity for estimating the solution to (33) is $\mathcal{O}(LKN_h \ln N_h)$, where L is the discretization parameter as used in (21), and $K = 6$ as observed below (29). In practice, the choice $L = 5$ is a good compromise between numerical accuracy and computation cost. Furthermore, the computation time of the HFM method can be deeply speeded up by exploiting a GPU-implemented scheme for estimating the geodesic distances, as proposed in (Mirebeau et al, 2023). The codes for the HFM method associated with the variant of the Euler-Mumford elastica model equipped with a curvature prior, involving the construction for the stencils, the computation for the geodesic distance map and the numerical solution to the geodesic backtracking ODE, can be downloaded from https://github.com/Mirebeau/HamiltonFastMarching.

References

Bakolas E, Tsiotras P (2009) On the generation of nearly optimal, planar paths of bounded curvature and bounded curvature gradient. In: 2009 American Control Conference, 2009 American Control Conference, pp 385–390, DOI 10.1109/acc.2009.5160269

Bardi M, Capuzzo-Dolcetta I (2008) Optimal control and viscosity solutions of Hamilton-Jacobi-Bellman equations. Birkhäuser Boston, MA, DOI 10.1007/978-0-8176-4755-1

Bekkers E, Duits R, Berendschot T, ter Haar Romeny B (2014) A multi-orientation analysis approach to retinal vessel tracking. Journal of Mathematical Imaging and Vision 49:583–610

Bekkers EJ, Duits R, Mashtakov A, Sanguinetti GR (2015a) A PDE approach to data-driven sub-Riemannian geodesics in SE(2). SIAM J Imag Sci 8(4):2740–2770

Bekkers EJ, Zhang J, Duits R, ter Haar Romeny BM (2015b) Curvature based biomarkers for diabetic retinopathy via exponential curve fits in se (2). In: Proc. Ophthalmic Med-

ical Image Analysis International Workshop, University of Iowa, vol 2

Bekkers EJ, Chen D, Portegies JM (2018) Nilpotent approximations of sub-Riemannian distances for fast perceptual grouping of blood vessels in 2D and 3D. J Math Imag Vis 60(6):882–899

Ben-Shahar O, Ben-Yosef G (2014) Tangent bundle elastica and computer vision. IEEE Trans Pattern Anal Mach Intell 37(1):161–174

Benmansour F, Cohen LD (2009) Fast object segmentation by growing minimal paths from a single point on 2D or 3D images. J Math Imaging Vis 33(2):209–221

Benmansour F, Cohen LD (2011) Tubular structure segmentation based on minimal path method and anisotropic enhancement. Int J Comput Vis 92(2):192–210

Caselles V, Kimmel R, Sapiro G (1997) Geodesic active contours. Int J Comput Vis 22(1):61–79

Cetin S, Demir A, Yezzi A, Degertekin M, Unal G (2012) Vessel tractography using an intensity based tensor model with branch detection. IEEE Trans Med Imag 32(2):348–363

Chambolle A, Pock T (2019) Total roto-translational variation. Numer Math 142(3):611–666

Chen D, Mirebeau JM, Cohen LD (2016) Finsler geodesics evolution model for region based active contours. In: Proc. BMVC

Chen D, Mirebeau JM, Cohen LD (2017) Global minimum for a Finsler elastica minimal path approach. Int J Comput Vis 122(3):458–483

Chen D, Zhang J, Cohen LD (2018) Minimal paths for tubular structure segmentation with coherence penalty and adaptive anisotropy. IEEE Trans Image Process 28(3):1271–1284

Chen D, Zhang J, Cohen LD (2019) Minimal paths for tubular structure segmentation with coherence penalty and adaptive anisotropy. IEEE Trans Image Process 28(3):1271–1284

Chen D, Cohen LD, Mirebeau JM, Tai XC (2021) An elastica geodesic approach with convexity shape prior. In: Proc. ICCV, pp 6900–6909

Cohen LD, Kimmel R (1997) Global minimum for active contour models: A minimal path approach. Int J Comput

Vis 24(1):57–78

Dijkstra EW (1959) A note on two problems in connexion with graphs. Numer Math 1(1):269–271

Duits R, Meesters SP, Mirebeau JM, Portegies JM (2018) Optimal paths for variants of the 2D and 3D Reeds–Shepp car with applications in image analysis. J Math Imag Vis 60(6):816–848

Franceschiello B, Mashtakov A, Citti G, Sarti A (2019) Geometrical optical illusion via sub-riemannian geodesics in the roto-translation group. Differ Geom Appl 65:55–77

Franken E, Duits R (2009) Crossing-preserving coherence-enhancing diffusion on invertible orientation scores. Int J Comput Vis 85:253–278

Hummel RA, Zucker SW (1983) On the foundations of relaxation labeling processes. IEEE Trans Pattern Anal Mach Intell (3):267–287

Jbabdi S, Bellec P, Toro R, Daunizeau J, Pélégrini-Issac M, Benali H (2008) Accurate anisotropic fast marching for diffusion-based geodesic tractography. Int J Biomed Imaging 2008:2

Kaul V, Yezzi A, Tsai Y (2012) Detecting curves with unknown endpoints and arbitrary topology using minimal paths. IEEE Trans Pattern Anal Mach Intell 34(10):1952–1965

Kimmel R, Sethian JA (2001) Optimal algorithm for shape from shading and path planning. J Math Imaging Vis 14:237–244

Kimmel R, Shaked D, Kiryati N, Bruckstein AM (1995) Skeletonization via distance maps and level sets. Comput Vis Image Underst 62(3):382–391

Lam L, Lee SW, Suen CY (1992) Thinning methodologies-A comprehensive survey. IEEE Trans Pattern Anal Mach Intell 14(09):869–885

Law MWK, Chung ACS (2008) Three Dimensional Curvilinear Structure Detection Using Optimally Oriented Flux. In: Proc. ECCV, pp 368–382

Li H, Yezzi A (2007) Vessels as 4-D curves: Global minimal 4-D paths to extract 3-D tubular surfaces and centerlines. IEEE Trans Med Imag 26(9):1213–1223

Liao W, Wörz S, Kang CK, Cho ZH, Rohr K (2018) Progressive minimal path method for segmentation of 2D and 3D line structures. IEEE Trans Pattern Anal Mach Intell 40(3):696–709

Melonakos J, Pichon E, Angenent S, Tannenbaum A (2008) Finsler active contours. IEEE Trans Pattern Anal Mach Intell 30(3):412–423

Mirebeau JM (2014a) Anisotropic fast-marching on cartesian grids using lattice basis reduction. SIAM J Numer Anal 52(4):1573–1599

Mirebeau JM (2014b) Efficient fast marching with Finsler metrics. Numer Math 126(3):515–557

Mirebeau JM (2018) Fast-marching methods for curvature penalized shortest paths. J Math Imag Vis 60(6):784–815

Mirebeau JM (2019) Riemannian fast-marching on Cartesian grids, using Voronoi's first reduction of quadratic forms. SIAM J Numer Anal 57(6):2608–2655

Mirebeau JM, Portegies J (2019) Hamiltonian fast marching: A numerical solver for anisotropic and non-holonomic eikonal pdes. Image Processing On Line 9:47–93

Mirebeau JM, Gayraud L, Barrère R, Chen D, Desquilbet F (2023) Massively parallel computation of globally optimal shortest paths with curvature penalization. Concurrency Computat, Pract Exper 35(2):e7472

Mumford D (1994) Elastica and computer vision. in Algebraic Geometry and Its Applications (C. L. Bajaj, Ed.), Springer-Verlag, New York, pages 491-506

Mumford D, Shah J (1989) Optimal approximations by piecewise smooth functions and associated variational problems. Commun Pure Appl Math 42(5):577–685

Nitzberg D M Mumford (1990) The 2.1-D Sketch*. In: Proc. ICCV, pp 138–144

Parent P, Zucker SW (1989) Trace inference, curvature consistency, and curve detection. IEEE Trans Pattern Anal Mach Intell 11(8):823–839

Parker GJ, Wheeler-Kingshott CA, Barker GJ (2002) Estimating distributed anatomical connectivity using fast marching methods and diffusion tensor imaging. IEEE Trans Med Imag 21(5):505–512

Péchaud M, Keriven R, Peyré G (2009) Extraction of tubular structures over an orientation domain. In: Proc. CVPR, pp 336–342

Peyré G, Péchaud M, Keriven R, Cohen LD (2010) Geodesic methods in computer vision and graphics. Foundations and Trends in Computer Graphics and Vision 5(3–4):197–397

Randers G (1941) On an asymmetrical metric in the four-space of general relativity. Phys Rev 59(2):195

Rouchdy Y, Cohen LD (2013) Geodesic voting for the automatic extraction of tree structures. Methods and applications. Comput Vis Image Underst 117(10):1453–1467

Saye R, Sethian JA (2012) Analysis and applications of the Voronoi implicit interface method. J Comput Phys 231(18):6051–6085

Saye RI, Sethian JA (2011) The voronoi implicit interface method for computing multiphase physics. Proc Nat Acad Sci 108(49):19,498–19,503

Sethian JA (1996) A fast marching level set method for monotonically advancing fronts. Proc Nat Acad Sci 93(4):1591–1595

Sethian JA (1999) Fast marching methods. SIAM Review 41(2):199–235

Sethian JA, Vladimirsky A (2001) Ordered upwind methods for static Hamilton–Jacobi equations. Proc Nat Acad Sci 98(20):11,069–11,074

Sethian JA, Vladimirsky A (2003) Ordered upwind methods for static Hamilton–Jacobi equations: Theory and algorithms. SIAM J Numer Anal 41(1):325–363

Siddiqi K, Bouix S, Tannenbaum A, Zucker SW (2002) Hamilton-jacobi skeletons. Int J Comput Vis 48(3):215–231

Türetken E, Benmansour F, Andres B, Głowacki P, Pfister H, Fua P (2016) Reconstructing curvilinear networks using path classifiers and integer programming. IEEE Trans Pattern Anal Mach Intell 38(12):2515–2530

Ulen J, Strandmark P, Kahl F (2015) Shortest paths with higher-order regularization. IEEE Trans Pattern Anal Mach Intell 37(12):2588–2600

Wertheimer M (1938) Laws of organization in perceptual forms (partial translation). In: A sourcebook of Gestalt Psychology, Kegan Paul, Trench, Trubner & Company, pp 71–88

Zhang J, Dashtbozorg B, Bekkers E, Pluim JP, Duits R, ter Haar Romeny BM (2016) Robust retinal vessel segmentation via locally adaptive derivative frames in orientation scores. IEEE Trans Med Imag 35(12):2631–2644